magnetochemistry

MDPI

Article

Structure, Microstructure, and Magnetic Properties of Melt Spun $Ni_{50}Mn_{50-x}In_x$ Ribbons

Karima Dadda [1,2], Safia Alleg [2], Joan Saurina [1], Lluïsa Escoda [1] and Joan-Josep Suñol [1,*]

[1] Campus Composites, University of Girona, C/Universitat de Girona 3, 17003 Girona, Spain; karima21@gmail.com (K.D.); joan.saurina@udg.edu (J.S.); lluisa.escoda@udg.edu (L.E.)

[2] Laboratoire de Magnétisme et Spectroscopie des Solides (LM2S), Département de Physique, Université Badji Mokhtar Annaba, B.P. 12, Annaba 23000, Algeria; alleg.safia@univ-annaba.org

* Correspondence: joanjosep.sunyol@udg.edu

Abstract: Structural, microstructural, and magnetic properties of Heusler $Ni_{50}Mn_{50-x}In_x$ (x = 5 and 10) ribbons have been investigated by X-ray diffraction (XRD), scanning electron microscopy (SEM) coupled with energy dispersive X-ray spectroscopy (EDS), differential scanning calorimetry (DSC), and vibrating sample magnetometry (VSM). The as quenched $Ni_{50}Mn_{45}In_5$ ribbons exhibit a mixture of monoclinic *14M* (a = 4.329(3) Å, b = 5.530(3) Å, and c = 28.916(3) Å), and tetragonal $L1_0$ (a = b = 3.533(3) Å, and c = 7.522(3) Å) martensite structures, while $Ni_{50}Mn_{40}In_{10}$ ribbons display a single monoclinic *14M* phase (a = 4.262(3) Å, b = 5.692(3) Å, and c = 29.276(3) Å). After three heating/cooling cycles, in the temperature range of 303–873 K, the Rietveld refinement of the XRD patterns revealed the presence of a single *14M* martensite for Ni50Mn45In5 ribbons, and a mixture of cubic $L2_1$ (31%) and *14M* (69%) phases for $Ni_{50}Mn_{40}In_{10}$ ribbons. The characteristic temperatures of the martensitic transition (A_{start}, A_{finish}, M_{start}, and M_{finish}), the thermal hysteresis temperature width, and the equilibrium temperature decreased with increasing indium content and heating cycles. The samples show a paramagnetic like behavior in the as quenched state, and a ferromagnetic like behavior after the third heating/cooling cycle.

Keywords: NiMn-based alloys; martensitic transition; XRD; thermal analysis; magnetic properties

Citation: Dadda, K.; Alleg, S.; Saurina, J.; Escoda, L.; Suñol, J.-J. Structure, Microstructure, and Magnetic Properties of Melt Spun $Ni_{50}Mn_{50-x}In_x$ Ribbons. *Magnetochemistry* **2021**, *7*, 63. https://doi.org/10.3390/magnetochemistry7050063

Academic Editors: Alexios Douvalis and Sabina Lesz

Received: 26 January 2021
Accepted: 1 May 2021
Published: 7 May 2021

1. Introduction

Great attention has been devoted to studying materials that show moderate magnetic entropy change values for their possible application as magnetic refrigerant materials near room temperature [1–3]. Off-stoichiometric Ni-Mn-Z (Z = Ga, In, Sn, Sb) Heusler alloys have several physical properties, such as magnetic shape memory, magnetocaloric effect, magnetic super-elasticity, exchange bias, and magnetoresistance [4–7]. Consequently, these alloys are of current interest due to their several technological applications as a magnetic coolant for magnetic refrigeration, magnetic actuated devices, and spintronic devices. Most of these functional properties are related to the first order magneto-structural transition from weak magnetic martensite to ferromagnetic austenite due to the strong magneto-structural coupling. The relationship between the magnetic and structural properties depends on the atomic ordering, outer electron to atom density (e/a), particle size, and preparation conditions [8,9]. The magnetic nature of the martensite in off-stoichiometric Ni-Mn based Heusler alloys is complex because the magnetic exchange is closely linked to the Mn-Mn interatomic distance. The magnetism is basically determined by the Mn magnetic moments through an indirect exchange interaction via conduction electrons [10]. The coupling between Mn atoms is very sensitive to the electron concentration and interatomic distance. Hence, the exchange coupling between Mn atoms in their regular sites is ferromagnetic (FM), whereas Mn atoms in the Ni and/or In anti-sites interact antiferromagnetically (AFM). Furthermore, due to the importance of the magnetic core/shell particles in electronics, composite materials, and catalysis [11], the effect of the exchange

interactions at interfaces between FM/AFM layers or between the core and the shell in NiMn-based alloys were investigated [12–14]. The stoichiometric Ni_2MnIn Heusler alloy crystallizes into a cubic $L2_1$ austenite structure with $Fm\bar{3}m$ space group. By lowering the temperature, the austenite structure undergoes a modulated and/or non-modulated martensitic phase transition. Usually, the non-modulated martensite has a body centred tetragonal (bct) crystal structure, and the modulated martensite might be orthorhombic or monoclinic. Basically, almost of the physical properties of materials are related to their microstructure and crystal structure [15], since the phase transition can be affected by the alloy composition, interatomic distances, and electronic band structure [16].

The effect of annealing on the chemical composition, atomic rearrangement, structural transition temperature, and magnetic properties in NiMn-based Heusler alloys has been largely explored [17,18]. The annealing of $Ni_{50.6}Mn_{36.3}Sn_{13.1}$ ribbons for 2 h at 550 °C leads to a reduction in the interatomic distances, an enhancement of the saturation magnetization, and strengthening of FM interactions [18]. Large magnetoresistance associated with a significant shift in the martensitic transformation temperature was observed in $Ni_{44.1}Mn_{44.2}Sn_{11.7}$ ribbons, after only 10 min of annealing at 850 °C [19]. By increasing the thermal treatment temperature, the martensitic transition temperature of $Ni_{48}Mn_{39.5}Sn_{9.5}Al_3$ ribbons increases and the exchange bias decreases. However, the effect of the thermal cycling on the thermal stability and magnetic properties has been less considered. Therefore, the present work was carried out to study the effect of heating/cooling cycles, in the temperature range of 303–873 K, on the structural stability and magnetic properties of the melt spun $Ni_{50}Mn_{45}In_5$ and $Ni_{50}Mn_{40}In_{10}$ Heusler ribbons. The main differences between the present work and those reported earlier are concerned with the heat treatment. For the isothermal conditions, the annealing is performed at a given temperature for a certain time. When the temperature is high, the time is relatively short and vice versa. This is the case of $Ni_{44.1}Mn_{44.2}Sn_{11.7}$ (800 °C, 10 min) and $Ni_{50.6}Mn_{36.3}Sn_{13.1}$ (550 °C, 2 h) ribbons. In our study, a cyclic heat treatment is performed in a temperature range. This is a non-isothermal heat treatment.

2. Materials and Methods

Polycrystalline $Ni_{50}Mn_{45}In_5$ and $Ni_{50}Mn_{40}In_{10}$ alloys, henceforth referred to as In5 and In10, respectively, were prepared by arc melting in a MAM-1 (Edmund Bühler GmbH, Bodelshausen, Germany) compact arc melter, in a water-cooled copper crucible under argon atmosphere from pure (99.98%) Ni, Mn, and In materials (Sigma Aldrich, Saint Louis, MO, USA). The ingots (5 g weight) were remelted several times to ensure a good homogeneity. The ribbons were obtained in a MSP10 melt spinning system (Edmund Bühler GmbH, Bodelshausen, Germany) under argon atmosphere (400 mbar) onto a polished surface of copper wheel rotating at a linear speed of 40 m/s, with a nozzle wheel distance of 3 mm, an orifice diameter of 0.5 mm, and an injection pressure of 500 mbar. The thickness, width, and length of the obtained ribbons were 15 μm, 1.5 mm, and 2–3 cm, respectively.

Structure and microstructure were investigated by X-ray diffraction (XRD) on a D8 Advance diffractometer (Siemens/Brucker, Billerica, MA, USA) in a θ–$2\,\theta$ Bragg Brentano geometry using Cu-Kα radiation (λ_{Cu} = 1.54056 Å) and scanning electron microscopy (SEM) Zeiss DSM-960A (Siemens/Brucker, Billerica, MA, USA) equipped with energy dispersive X-ray spectrometry (EDS), respectively. The average crystallite size, <L>, root-mean square (r.m.s.) microstrains, $<\sigma^2>^{1/2}$, lattice parameters (a, b, c), β angle, and phase proportion (percentage) were obtained from the Rietveld refinement of the XRD patterns by the MAUD program (University of Trento, Trento, Italy) [20] which is based on the Rietveld method [21]. The XRD measurements have been performed on the powder for the heat-treated HT3-In5, and HT3-In10 samples, and on the free and wheel surfaces together for the as quenched ribbons (AQ-In5 and AQ-In10).

Thermal analysis was studied by differential scanning calorimetry (DSC) in a DSC Q2000 (TA Instruments, New Castle, DE, USA) in the temperature range of 303–873 K at a heating/cooling rate of 20 K/min. In order to check the thermal stability of the produced ribbons, one, two, and three heating/cooling cycles were performed on the In5 and In10

samples, and the heat-treated samples were named HT1-In5, HT2-In5, HT3-In5, HT1-In10, HT2-In10, and HT3-In10, respectively. The hysteresis loops of the as quenched and heat-treated samples were measured in a vibrating sample magnetometer (VSM) LakeShore 7404 (Lake Shore, Westerville, OH, USA) at room temperature (300 K) under maximum external magnetic field of 20 kOe.

3. Results and Discussion

3.1. Structure

The XRD patterns of the as quenched (juxtaposed F and W sides) and heat-treated (powders) In5 and In10 ribbons at room temperature, contain many diffraction peaks in the 2θ range of 39–48° characteristic of the martensitic structure (Figure 1). The peak broadening of the as quenched ribbons might be correlated to the atomic disorder that is induced during the rapid solidification. Moreover, the difference between the XRD patterns of AQ (Figure 1a), HT3 (Figure 1b), and AQ/HT3 (Figure 1c,d) ribbons can be attributed to the indium content, preferred orientations (texture), internal stresses, crystallographic structure, and phase's formation/transformation. For example, the crystallographic structure changes might be attributed to the indium content and heat treatment as shown in Figure 1a,b, while the variation in the peak intensities can be related to the texture in the as quenched state (Figure 1c,d). The preferential orientation is favored by the existence of columnar grains between both W and F sides of ribbons. Furthermore, the enhanced reflection intensities of the heat-treated ribbons can be ascribed mainly to the reduction of internal stresses and structural defects. Additionally, the structural transformation is evidenced by the appearance of new diffraction peaks, as indicated by symbols in Figure 1c,d, for HT3-In5 and HT3-In10, respectively. Accordingly, the Rietveld refinement was performed by using either a single or two phases.

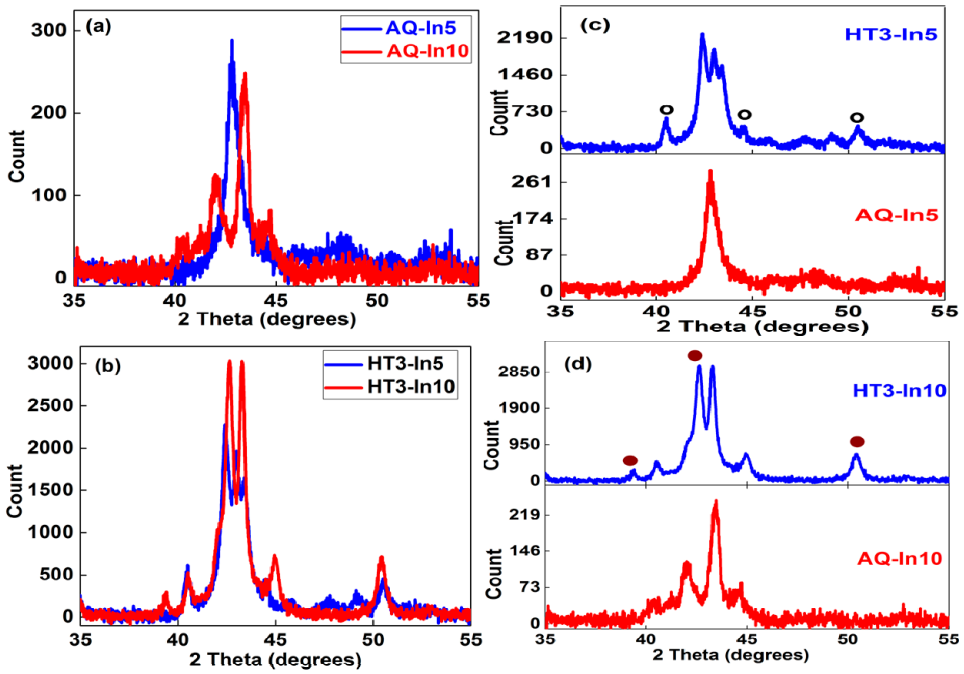

Figure 1. XRD patterns of AQ-In5/AQ-In10 (**a**), HT3-In5/HT3-In10 (**b**), AQ-In5/HT3-In5 (**c**), and AQ-In10 /HT3-In10 (**d**) samples, in the 2θ range of 35–55°, showing the effect of the composition and/or heat treatment.

Figure 2 shows the Rietveld refinement of the XRD patterns, whereas the alloys from the top to bottom are AQ-In5, HT3-In5, AQ-In10, and HT3-In10, respectively. For the as quenched samples, the Rietveld refinement reveals the coexistence of the non-modulated $L1_0$ (≈86%) and modulated *14M* (≈14%) martensite structures for the AQ-In5, and a single modulated *14M* structure for the AQ-In10. The formation of the martensite structures

in both alloys can be related to the fast solidification from the melt that yields a rapid crystallization, and implies the existence of a greater amount of structural defects, such as point defects, dislocations, grain boundaries, stacking faults, etc. Moreover, the thermal gradient between the wheel and free surfaces of the ribbons gives rise to internal stresses. Furthermore, the coexistence of two martensitic phases in the AQ-In5 can be attributed to the rapid solidification from high temperature, and the closeness of their stability.

The non-modulated $L1_0$ has a tetragonal structure belonging to space group *P4/mmm*, and the modulated *14M* has a monoclinic structure belonging to space group $P2_1/m$. The illustration of tetragonal $L1_0$ and monoclinic *14M* crystal structures are displayed in Figure 3. The face centered tetragonal $L1_0$ structure is derived from the *B2* phase by the distortion of the cubic lattice formed without modulation. Thus, the appearance of $L1_0$ martensite in the AQ-In5 ribbons can be related to the high level of internal stresses and defects. Furthermore, the formation of the modulated *14M* martensite structure can be attributed to the reduction of the constraint stress which is introduced during the structural transition from the *B2* to *14M* structures through the volume change. The modulation might be necessary to accommodate the martensitic domain on the interface (habitat plane) between the martensite and austenite, which is invariant across the structural transition, to keep low transformation energy [22]. Several structures can exist in the modulated and non-modulated martensite depending on the chemical composition, temperature, and production method. Indeed, the obtained result regarding the coexistence of the $L1_0$ and *14M* martensite structures in the AQ-In5 sample is different from those reported for the $Ni_{50}Mn_{45}In_5$ alloys prepared by arc melting followed by annealing at 1073 K for 2 h [5] and 5 days [12], where a single $L1_0$ martensite structure was obtained. Those differences might be attributed to the higher density of structural defects (mainly dislocations) in the rapid quenched materials compared to that in the arc-melted bulk materials [23]. The inhomogeneous behavior of the melt-spun ribbons might be associated with the high level of internal stresses due to the constraint effect among solidified areas at different temperatures. Consequently, some areas transform at higher/lower temperatures and some other regions remain untransformed, even upon further cooling. Besides, the structure of the transformed zones fluctuates spatially from faulted $L1_0$ to faulted *14M* with a changeable periodicity.

The XRD patterns of the heat-treated samples (HT3-In5 and HT3-In10) reveal the presence of a modulated martensite structure. Furthermore, the increase of the diffraction peaks intensity and their narrowing after the third heating/cooling cycle might be attributed to the reduction of internal stress, atomic disorder, and defects, as well as to the increase of the crystallite size of the *14M* martensite structure (Table 1). Besides, the disappearance of the $L1_0$ peaks and the emergence of new reflections on either side of the main diffraction peak can be attributed to the transformation of the tetragonal $L1_0$ to monoclinic *14M* structure in the case of HT3-In5 ribbons. However, in the case of the HT3-In10 ribbons, the XRD pattern displays, in addition to the same Bragg peaks as those of AQ-In10 ribbons in the 2θ range of 39–48°, the presence of new peaks at about 39.37°, 42.63°, and 50.55° characteristic of the cubic $L2_1$ structure. The Rietveld refinement of the XRD patterns was achieved with a single *14M* structure for the HT3-In5, and a mixture of *14M* and $L2_1$ structures for the HT3-In10 ribbons (Figure 2). The obtained results from the Rietveld refinement are summarized in Table 1. The $L1_0 \rightarrow 14M$ phase transformation might be allowed by the reduction of internal stresses and defects. Upon heating/cooling cycles, the thermal stress slithers the atomic planes of the tetragonal $L1_0$ structure in order to form the monoclinic *14M*. In Ni-Al melt-spun materials, it has been reported that the formation of the *14M* structure is controlled by both the Ni content and local stress configuration existing between the transformed and untransformed areas. Furthermore, the 14*M* structure is stable in areas with a slightly higher Ni content (below 63 at.%), while the Ll_0 structure is stable in areas with the highest Ni-content (above 63 at.%) [24]. The formation of the cubic $L2_1$ structure in the HT3-In10 ribbons can be ascribed to the increase of atomic order degree, and to the presence of In-rich region. Indeed, the Ni-Mn-In alloys exhibit an austenitic structure at room temperature, for higher indium content (above 10%).

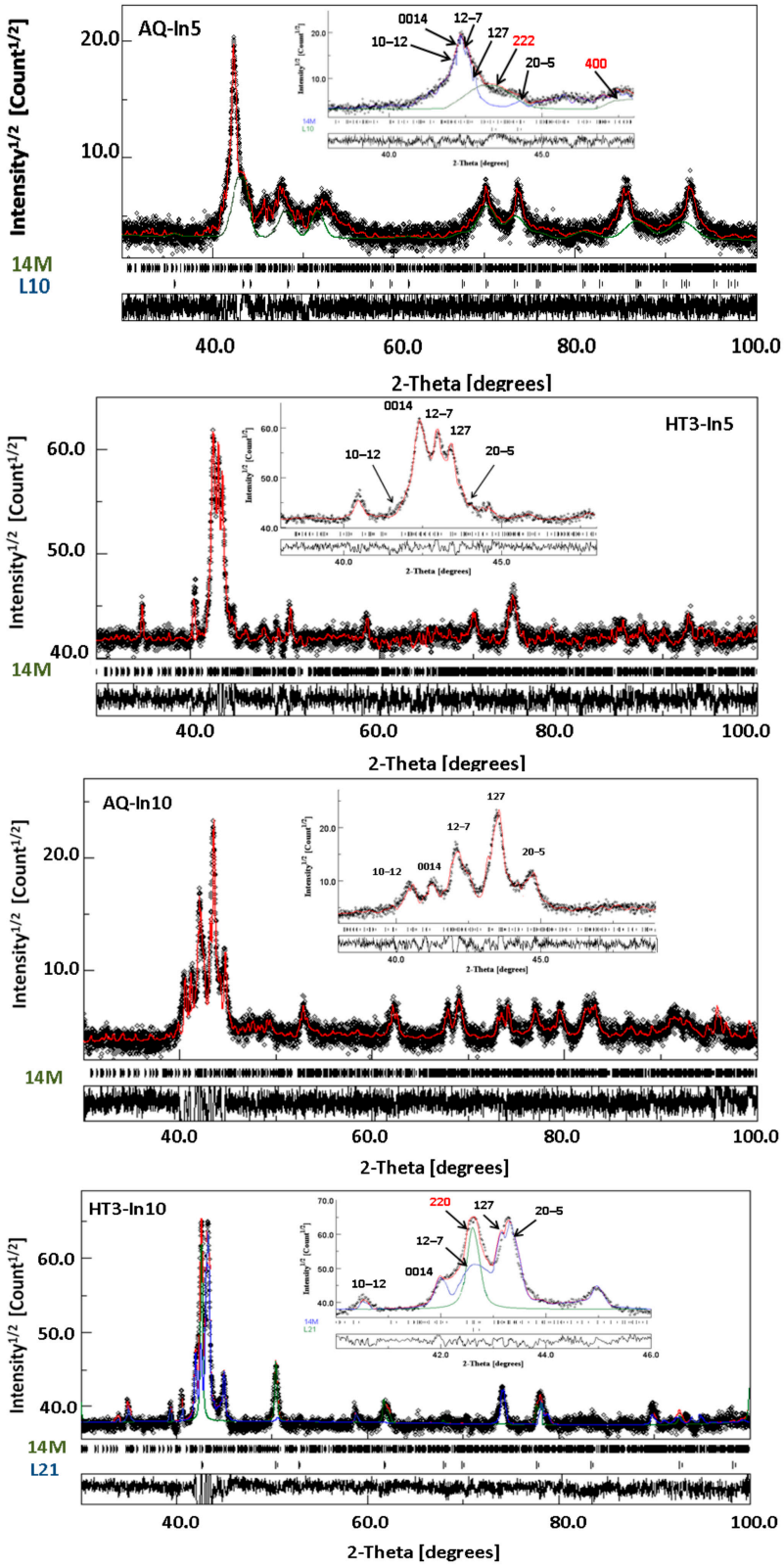

Figure 2. Rietveld refinement of the XRD patterns of the as quenched (AQ-In5 and AQ-In10) and heat-treated (HT3-In5 and HT3-In10) samples. The difference between the measured (dots) and calculated (line) patterns is shown below (Diff.). The reliability factors are G_{of} = 1.2, Rwp(%) = 25.17, Rb(%) = 19.06, and Rexp(%) = 22.27 for AQ-In5; G_{of} = 1.4, Rwp(%) = 3.94, Rb(%) = 2.87, and Rexp(%) = 1.95 for HT3-In5; G_{of} = 1.35, Rwp(%) = 3.25, Rb(%) = 2.3, and Rexp(%) = 2.32 for AQ-In10; Gof = 1.26, Rwp(%) = 4.6, Rb(%) = 3.14, and Rexp(%) = 2.6 for HT3-In10. The insets show the enlargement of the 2θ range of 39–46°.

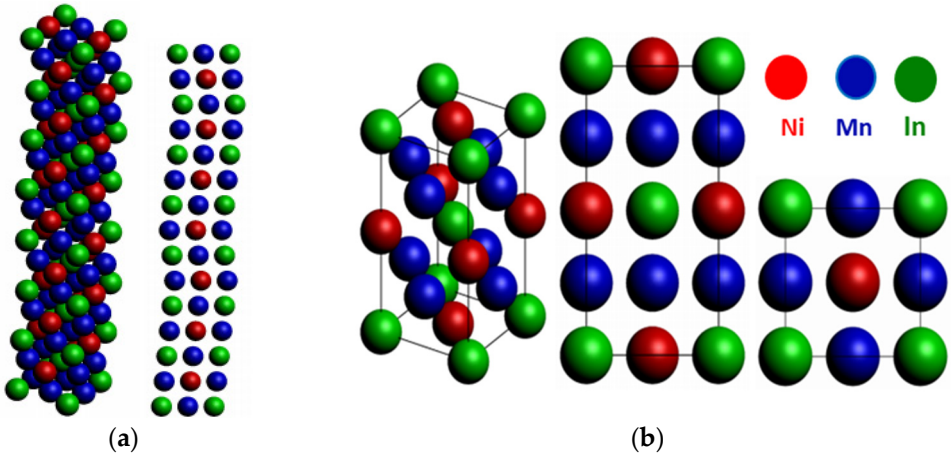

Figure 3. Illustration of monoclinic *14M* (**a**) and tetragonal $L1_0$ (**b**) crystal structures.

Table 1. Structure, lattice parameters (a, b, c), β angle, average crystallite size, <L>, microstrains, $<\sigma^2>^{1/2}$, and relative fraction of AQ-In5, AQ-In10, HT3-In5, and HT3-In10 ribbons.

Sample	Structure	a (Å)	b (Å)	c (Å)	β (°)	Fraction ± 2 (%)	<L> ± 5 nm (nm)	$<\sigma^2>^{1/2}$ ± 0.01
AQ-In5	$L1_0$	3.533(3)	3.533(3)	7.522(3)	90.00	86	145	0.60
	14M	4.329(3)	5.530(3)	28.916(3)	93.04	14	97	0.06
HT3-In5	*14M*	4.293(3)	5.606(3)	29.043(3)	92.78	100	100	0.06
AQ-In10	*14M*	4.262(3)	5.692(3)	29.276(3)	92.98	100	82	0.06
HT3-In10	*14M*	4.253(3)	5.147(3)	29.605(3)	89.3	69	100	0.06
	$L2_1$	6.069(3)	6.069(3)	6.069(3)	90.00	31	99	0.06

The average crystallite size of the *14M* martensite decreases with increasing indium content from 97 nm to 82 nm for the AQ-In5 and AQ-In10 ribbons, respectively, while it increases to about 100 nm, after the third heating/cooling cycle for both alloys. Likewise, the average crystallite size of the non-modulated $L1_0$ martensite (145 nm) is higher than that of the modulated *14M* martensite (97 nm). This is in agreement with the fact that the amount of martensite increases with the crystallite size growth [25]. Moreover, the $L1_0$ martensite has higher microstrains (≈60%) than the *14M* martensite (≈6%) and $L2_1$ austenite (≈6%). Indeed, both $L1_0$ and 14*M* phases have a lamellar microstructure, but the lamellae in the *14M* phase are thinner than those in the $L1_0$ one. Therefore, a large interfacial energy is generated in the non-modulated martensite variant because of its thick lamellae, which increase the internal stresses and the microstrains rate [26].

The lattice parameters of the *14M* structure vary as a function of indium content and heat treatment. For the AQ-In10, the lattice parameters are lower than those of the $Ni_{50}Mn_{40}In_{10}$ bulk alloy [5], while the lattice parameters of the $L1_0$ are different from those reported for the $Ni_{50}Mn_{45}In_5$ alloys [5,27]. The discrepancies between the present results and those reported earlier might be ascribed to the experimental conditions, such as the preparation method, alloy composition, and heat treatments (time and temperature), that can influence the structure, phase transformation, structural defects, lattice parameters, crystallite sizes, etc. For example, the prepared materials by melt spinning process present a crystallite size refinement, directional growth (texture), atomic disorder, and high level of internal stresses that can be relaxed by annealing.

3.2. Morphology

Figure 4 displays typical SEM images revealing the morphologies of the free surface (F), wheel surface (W), and cross section of the as-spun In5 and In10 ribbons. The morphology of the F and W surfaces differs considerably since W surface had contact with the wheel, while the F surface shows the upper ("free") side. The microstructure of the free surface exhibits plate-like morphology characteristic of martensitic structure, while the wheel surface

morphology consists of columns disposed parallel to the surface. The ribbons morphology can be described by the ordered columnar microstructure that is disposed perpendicularly to the ribbons plane from thin layer of small grains on the wheel surface, showing the directional growth of the crystalline phase formed after heat removal by melt spinning technique. The free surface exhibits characteristic elongated thin plates corresponding to martensite variants. The In5 and In10 ribbons show different microstructures that can be linked to the martensite variants. It is important to mention that there is a difference between the crystallite size or coherent diffraction domains analysis in the XRD data, and the grain analysis for the SEM data. Furthermore, since the martensite exhibits a lamellar structure, it is therefore difficult to observe the grains in the SEM micrographs of the as quenched samples.

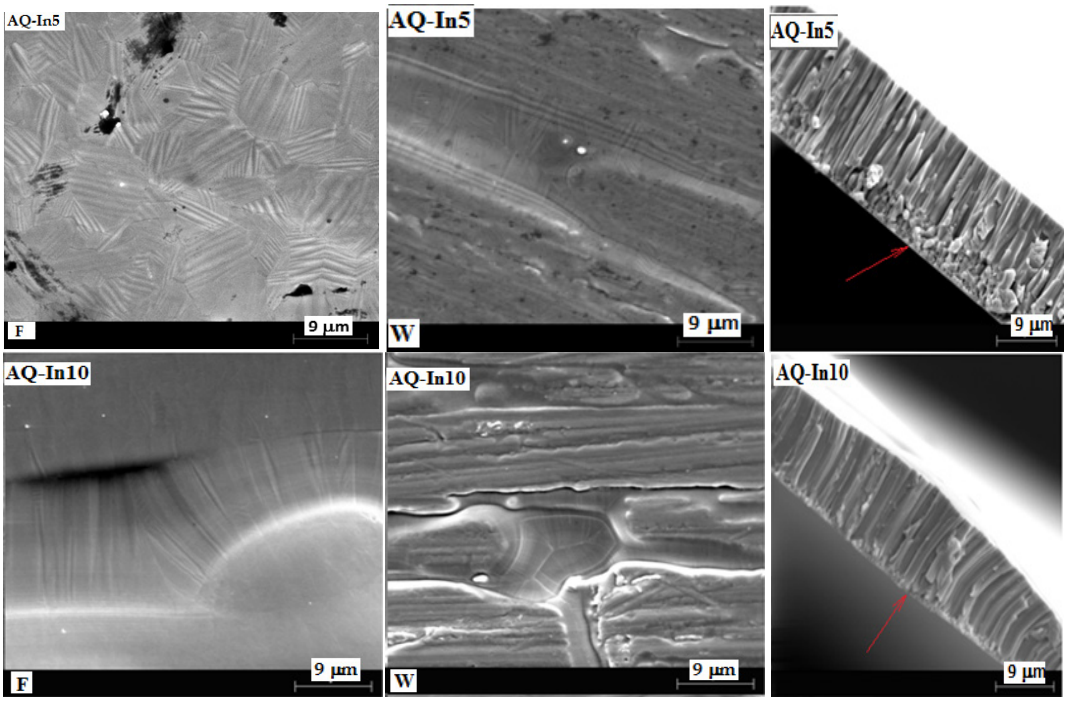

Figure 4. SEM micrographs of the free surface (**F**), wheel surface (**W**), and cross section (**right**) of the AQ-In5 and AQ-In10 ribbons. The red arrow indicates the wheel contact surface.

The SEM morphologies of the heat-treated ribbons (HT1-In5, HT3-In5, HT1-In10, and HT3-In10) show different microstructure compared to that of the as quenched samples (Figure 5). Indeed, in addition to the plate like morphology of the martensite (Figure 5c,d), some regions reveal the presence of very small grains with spherical shape (Figure 5e). Those differences might be linked to the variation of the martensite plate's width, and the formation of new precipitates, as indicated by the circles. Such morphology might be correlated to the formation of the cubic $L2_1$ austenite structure in the HT3-In10 ribbons and thus confirms the XRD results. One expects that this microstructure change might affect the magnetic properties, such as the coercivity and saturation magnetization of the heat-treated samples. Moreover, this change in microstructure indicates a variation of the martensitic structure amount, and consequently, it may lead to a change in the martensitic phase transition temperature.

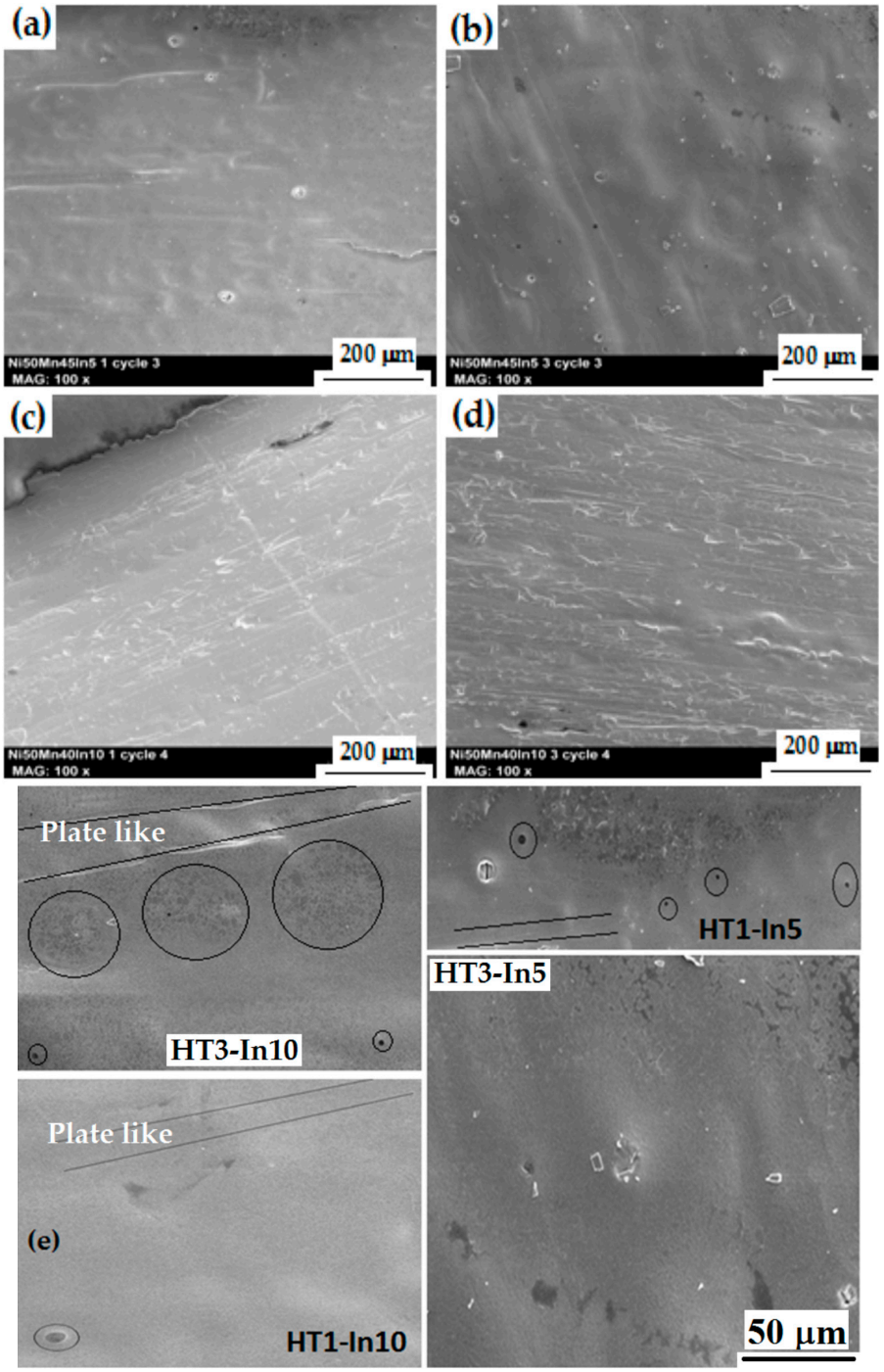

Figure 5. SEM micrographs after one and three heating/cooling cycles in the In-5 and In-10 samples: (**a**) HT1-In5; (**b**) HT3-In5; (**c**) HT1-In10; and (**d**) HT3-In10 ribbons. The enlargement parts (**e**) reveal different morphologies.

The elemental composition of the as quenched and heat-treated ribbons was performed by energy dispersive X-ray spectrometry (EDS). To check the homogeneity of the samples, the EDS spectra were taken from six different regions. The obtained results are collected in Table 2. The atomic concentration ratio of the valence electrons, of which nickel has 10, manganese 7, and indium 3, is calculated according to the following relationship:

$$e/a = \frac{10 \times \text{Ni.at\%} + 7 \times \text{Mn.at\%} + 3 \times \text{In.at\%}}{100} \quad (1)$$

where Ni.at%, Mn.at%, and In.at% are the average atomic concentrations obtained for each element. The elemental analysis (Table 2) shows a slight variation of Ni, Mn, and In proportions. Those deviations might be related to the heterogeneities of the melt spun ribbons, and/or to the evaporation of Mn and In during the melting process, since their evaporation enthalpies are lower than that of the Ni (ΔH_{Mn} (226 KJ/mol) < ΔH_{In} (232 KJ/mol) < ΔH_{Ni} (370 KJ/mol). The corresponding atomic concentration ratios of In5 (8.34–8.37) and In10 (8.13–8.27) are slightly higher than the theoretical ones (8.3 for In5 and 8.1 for In10). Such divergence might influence the martensitic transformation temperature, which can be twinned by the *e/a* ratio, Mn nearest neighbor interatomic distances, atomic order degree, and crystallite size [28,29]. Furthermore, the ratio decreases with increasing indium content, as expected.

Table 2. Elemental analysis and *e/a* ratio (theoretical and experimental) of the as quenched and heat-treated In5 and In10 ribbons.

Element (at.%)	In5			In10		
	AQ-In5	**HT1-In5**	**HT3-In5**	**AQ-In10**	**HT1-In10**	**HT3-In10**
Ni	52.3	52.7	51.2	51.4	54.0	52.0
Mn	43.0	42.6	44.0	38.3	36.0	38.7
In	4.7	4.7	4.8	10.3	10.0	9.3
$(e/a)_{theo}$	8.30	8.30	8.30	8.10	8.10	8.10
$(e/a)_{exp}$	8.37	8.39	8.34	8.13	8.27	8.18

3.3. Thermal Analysis

Three successive DSC scans were performed on the In5 and In10 samples, as shown in Figure 6. The produced ribbons exhibit a martensitic transition, above the room temperature, characterized by an endothermic peak on heating and an exothermic peak on cooling. Additionally, as the number of the heating/cooling cycle increases, the height of the endothermic and exothermic peaks decreases (weak peaks), the transformation temperature varies, and the transformation region is reduced. Consequently, the area under the peak decreases from 44 J/kg K to 39 J/kg K to 29 J/kg K after the first, second, and third cycles, respectively, during the cooling of the In5 ribbons. The same trend is observed for the In10 ribbons where the area under the peak is about 39 J/kg K, 21 J/kg K, and 12.5 J/kg K for the first, second, and third cycles, respectively. The reduction of the area under the DSC peaks might be related to the structural evolution of the alloys. The important decrease in the entropy of the In-10 ribbons can be related to the rise in the atomic order. Undoubtedly, the increase of atomic order degree stabilizes the austenite and leads, thus, to the reduction of the entropy and the shift of the martensitic transition temperature. Indeed, if the alloy structure is cubic, the austenite to martensite transition must be found below room temperature; while it is above room temperature if the phase structure is tetragonal, monoclinic, or orthorhombic. Hence, the formation of the $L2_1$ austenite phase in the HT3-In10 ribbons might explain the important reduction of the peaks areas of the In-10 compared to those of the In5 ribbons. The decrease of the area under the peaks can be thus correlated to the reduction of the amount of the martensite, which might be confined to a small portion of the total volume as well as to the local composition heterogeneities. Furthermore, the difference between the In5 and In10 behavior can be related to the structural state of the as quenched ribbons.

The characteristic temperatures of the structural transition are denoted as martensite start, M_{start}, martensite finish, M_{finish}, austenite start, A_{start}, and austenite finish, A_{finish} (Table 3). The martensitic transformation temperature decreases with increased indium content and the number of heating/cooling cycles. The transformation region can be characterized by the equilibrium temperature ($T_0 = \frac{M_{start}+A_{finish}}{2}$), at which the Gibbs energies of the martensite and austenite phases are equal. The slight decrease of M_{start} temperature in In5 ribbons might be linked to the disappearance of the $L1_0$ structure after

annealing. The width of the thermal hysteresis is an important parameter that describes the structural transformation. It is defined as follows:

$$\Delta T_{hys} = A_p - M_p \quad (2)$$

where A_p and M_p are the forward and reverse structural transition peak temperatures given by $A_p = \frac{A_{start}+A_{finish}}{2}$ and $M_p = \frac{M_{start}+M_{finish}}{2}$. The decrease of the thermal hysteresis width, ΔT_{hys}, from 71 to 62.5 K to 61 K for In5, and from 60 to 34 K to 14 K for In10 after the first, second, and third cycles, respectively, is partly due to the removed defects and released internal stresses. Those effects are considered to increase the equilibrium transformation temperature, $T_m = \frac{A_{start}+M_{finish}}{2}$ [30]. Besides, the annealing increases the degree of atomic order, which leads to the decrease of T_m. Accordingly, the reduction of T_m can be related to the decrease in the structural order effect and the composition change, which affect the electron-to-atom ratio and leads, hence, to a change in the $d_{Mn} - d_{Mn}$ interatomic distances. It is important to note that the high heating/cooling rate, leads to over/underestimated finish temperatures.

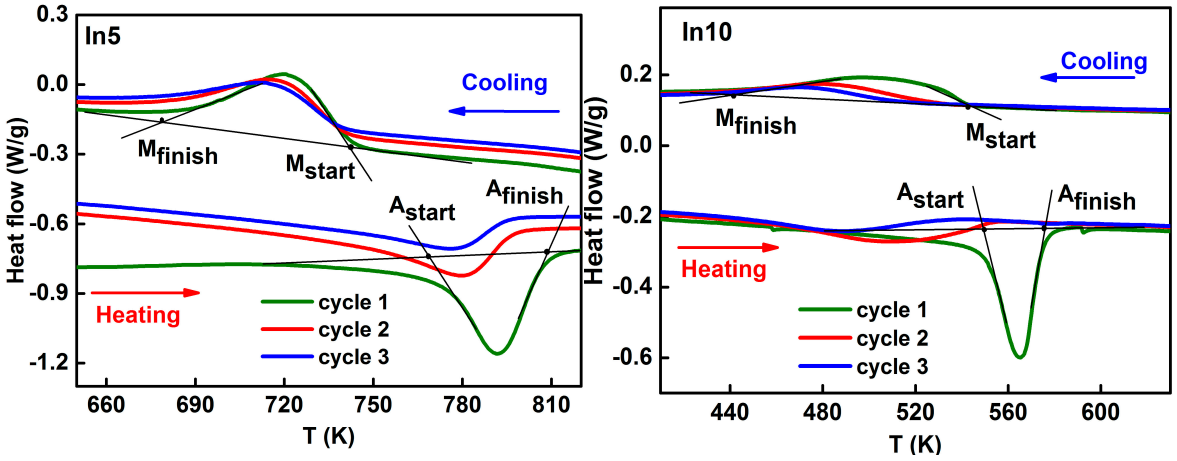

Figure 6. Three successive DSC scans of the AQ-In5 and AQ-In10 ribbons at a heating/cooling rate of 20 K/min.

Table 3. The measured characteristic transformation temperatures (A_{start}, A_{finish}, M_{start}, and M_{finish}), the calculated equilibrium (T_0), and thermal hysteresis (ΔT_{hys}) temperatures.

Samples	**In5**			**In10**		
Cycles	**1**	**2**	**3**	**1**	**2**	**3**
A_{Start} (K) $\pm$ 2	771	733	717	550	452	438
A_{finish} (K) $\pm$ 2	812	825	834	581	581	537
M_{Start} (K) $\pm$ 2	743	740	739	543	528	512
M_{finish} (K) $\pm$ 2	698	693	690	468	437	435
$T_0(K) \pm 2$	734.5	713	703.5	509	444.5	436.5
ΔT_{hys} (K) $\pm$ 2	71	62.5	61	60	34	14

3.4. Magnetic Measurements

Figure 7 shows the hysteresis loops, at room temperature, of the as quenched and heat-treated In5 and In10 ribbons, after one and three heating/cooling cycles in the temperature range of 303–873 K. For the AQ-In5 and AQ-In10 ribbons, the variation of the magnetization as a function of the applied magnetic field, M(H), exhibits nearly straight lines characteristic of a paramagnetic (PM) like behavior due to the weakly magnetic martensite, and to the local atomic disordering which leads to the FM coupling loss. The local atomic disordering is a characteristic of the rapid quenching process. Hence, the stronger paramagnetic signal in the AQ-In10 can be due to the structural state. Besides, the M(H) curves display a

negative vertical shift (Figure 7a) that can be ascribed to the strong AFM interactions in the martensite structure, and/or to the short-range AFM coupling in the Mn-rich areas.

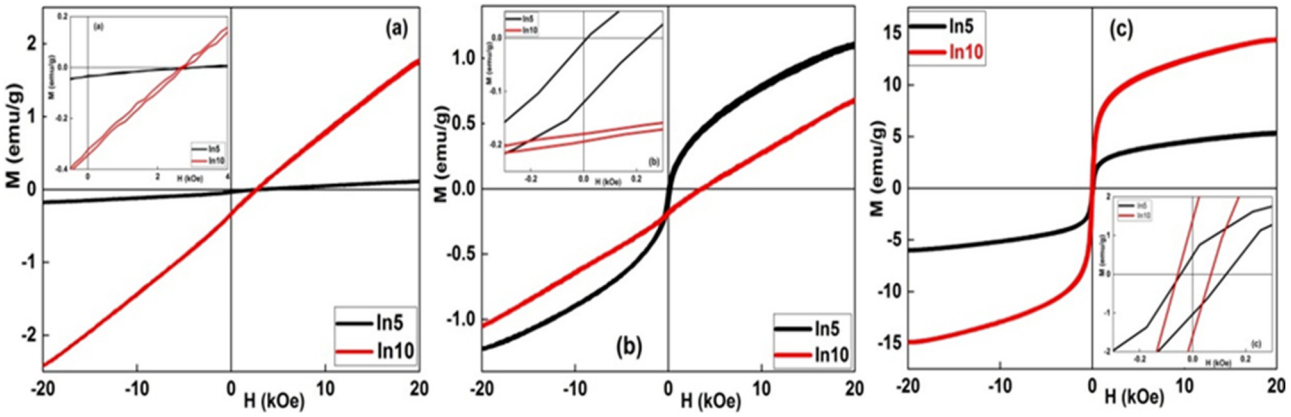

Figure 7. Hysteresis loops, at 300 K, of the as quenched (**a**) and heat-treated In5 and In10 samples after one, (**b**) and three (**c**) heating/cooling cycles. The inset shows the central part enlargement.

After one heating/cooling cycle (Figure 7b), the In10 sample shows also nearly a straight line, but with reduced negative shift of the magnetization compared to the as quenched sample. However, the M(H) curve of the In5 ribbons reveals a ferromagnetic like behavior with a positive horizontal shift. This later can be associated to the spin reconfiguration at the interface AFM and FM species giving rise to an exchange bias (EB) like behavior at room temperature. Furthermore, after the third heating/cooling cycle (Figure 7c), both samples show a ferromagnetic like behavior. The discrepancies between the magnetic behavior of the two samples after the first heating/cooling cycle can be ascribed to the crystallographic structure of the as quenched state, since the melt spinning process leads to a monophasic and biphasic structures for the AQ-In5 and AQ-In10, respectively. Further heating/cooling cycles (HT3 cycle), lead to an important change in the hysteresis loops that can be correlated to the structural order. Additionally, the change from the PM like to the FM like behavior might be due to the formation of locally FM nano-sized precipitates in the AFM matrix. Additionally, the increase of the samples' magnetization after cyclic heat treatment can be associated to the decrease of the AFM coupling between Mn atoms due to the decrease of the density of antiphase boundaries as an outcome of the dislocation annihilation. Likewise, the diminution of the non-magnetic inclusions/defects density as well as their stress field, gives rise to an increase in the magnetization, and a decrease of the martensitic transition temperature range, respectively. The improved FM like behavior in the HT3-In10 sample (Figure 7c) can be linked to the increase in long range atomic order since it has a direct influence on the magnetic exchange coupling between Mn atoms. Additionally, the FM like behavior can be related to the formation of $L2_1$ austenite and the reduction of the weakly magnetic martensite, and thus confirms the XRD results.

The coercive fields (defined as $Hc = (H_1 - H_2)/2$, where H_1 and H_2 are left and right fields at which the magnetization equals to zero, respectively) are of about 86 Oe and 63 Oe for the HT3-In5 and HT3-In10 ribbons, respectively. The decrease of the coercivity from 115 to 63 Oe for the AQ-In5 and HT3-In5, respectively, can be linked to the structural relaxation and the reduction of the structural defects. The PM like behavior can be attributed to the structural disorder, and/or short-range order in the melt-spun ribbons since the magnetic coupling is very sensitive to the atomic distances in NiMn-based Heusler alloys. Furthermore, the vertical shift in the magnetization curves might be ascribed to the strong AFM interactions in the martensite and/or to the short-range AFM magnetic coupling in the Mn-rich areas, knowing that the fast solidification leads to structural heterogeneities, owing to the temperature difference between the free and wheel surfaces of the ribbons. The

negative shift of the hysteresis loops has been observed in the annealed off-stoichiometric $Ni_{49.6}Mn_{45.5}In_5$ sample at temperatures between 650 and 750 K under a magnetic field of about 0.1 T [12]. It has been reported that the compound decomposes into FM nano-precipitates embedded in a $Ni_{50}Mn_{50}$ AF matrix at room temperature. Additionally, the negative shift of the magnetization in the Ni-Mn-In shell FM nano-precipitates has been attributed to the occurrence of the magnetic proximity effect, whereby the interfacial spins align along the field applied during segregation [31]. The spins at the interface with the NiMn matrix align with the annealing field during their growth and become strongly pinned in the field direction during annealing, forming the so-called shell ferromagnet.

The horizontal shift of the M(H) curves can be related to the development of magnetically non-homogeneous AF/FM matrix where the interfacial pinning of FM spins by the AF component gives rise to an exchange bias (EB) like behavior at room temperature. Hence, the EB effect can be attributed to a FM unidirectional anisotropy (texture) formed at the interface between different magnetic phases upon the fast solidification process of the ribbons by melt spinning. This result is different from those reported in the literature concerning the EB in the bulk Ni-Mn-In system, where it is usually observed in the Mn-rich alloys at low temperature, when the system is cooled under an applied magnetic field through its blocking temperature [32]. Consequently, by using the melt spinning process and a thermal cycling up to a relatively lower temperature than those reported in the literature, the EB has been observed in the hysteresis loops at room temperature.

The magnetic properties in off-stoichiometric Ni-Mn-Z Heusler alloys are mainly related to Mn-Mn interactions. Indeed, the excess of Mn atoms increases the Ni(3d)-Mn(3d) hybridization and strengths of the AFM interactions. Consequently, the AF coupling between Ni-Mn atoms and between the extra Mn and the Mn atoms at the ordinary sites reduces the magnetization. Hence, the increase of the magnetization for both samples, after the third heating/cooling cycle, can be attributed to the change of the AF coupling between Mn-Mn atoms to FM coupling. This may also be linked to the increase in the ordering of Ni–Ni moments. Moreover, the expansion of the unit cell volume through the distortion of the crystalline lattice can be linked to the replacement of the Mn atoms by In ones since the atomic radius of indium is greater than that of the manganese ($r_{In} = 0,142\ nm > r_{Mn} = 0,126\ nm$). This might enhance the ferromagnetism.

4. Conclusions

The effect of thermal heating/cooling cycles on the structure, microstructure, and magnetic properties of Heusler In5 and In10 ribbons were investigated. The obtained results can be summarized as follows:

- The Rietveld refinement reveals a mixture of tetragonal $L1_0$ (86%) and monoclinic *14M* (14%) martensite structures for the AQ-In5 ribbons and a single *14M* structure for the AQ-In10 ribbons.
- After the third heating/cooling cycle, in the temperature range of 303–873 K, the HT3-In5 sample exhibits a single *14M* structure, while the HT3-In10 sample shows a mixture of *14M* (69%) and cubic $L2_1$ (31%) structures.
- The crystallite sizes of the AQ and HT3 samples are in the nanoscale level.
- The small deviations of Ni, Mn, and In concentrations from the theoretical composition are partly due to the heterogeneities in the produced ribbons.
- The characteristic temperatures of the martensitic transition decrease with increasing In content and the heating/cooling cycles.
- The In5 and In10 samples show a paramagnetic like behavior in the AQ state and a ferromagnetic like behavior after the third heating/cooling cycle.
- By using the melt spinning process and a thermal cycling up to a relatively lower temperature than those reported in the literature, an EB was observed in the hysteresis loops at room temperature.

Author Contributions: Conceptualization, S.A. and J.-J.S.; formal analysis, K.D. investigation, L.E. and J.S.; writing—original draft preparation, K.D.; supervision, S.A. and J.-J.S. All authors have read and agreed to the published version of the manuscript.

Funding: The authors gratefully acknowledge the support from DGRSDT/MESRS Algeria, Spanish MINECO project MAT2016-75967-P, UdG project PONTOS 2020/01, and the Erasmus+k107 STA program.

Data Availability Statement: Data can be requested to the authors.

Acknowledgments: The authors agree technical support from "Serveis Tècnics de Recerca" of the University of Girona. The authors want to thank Foued Khammassi from the LM2S Laboratory for the VSM measurements.

Conflicts of Interest: The authors declare no conflict of interest.

References

1. Jemmali, M.; Nouri, K.; Walha, S.; Benali, A.; Ben Salah, A.; Dhahri, E.; Bessais, L. Effect of small Fe content on the structure, magnetic, and magnetocaloric properties of $SmNi_{3-x}Fe_x$ (x= 0; 0.3 and 0.8) Intermetallic Compounds. *J. Supercond. Nov. Magn.* **2018**, *31*, 511–520. [CrossRef]
2. El-Sayed, A.H.; Hamad, M.A. Phenomenological modeling of magnetocaloric effect for $Ni_{58}Fe_{26}Ga_{28}$ alloy. *J. Supercond. Nov. Magn.* **2018**, *31*, 1895–1898. [CrossRef]
3. Khlifi, M.; Dhahri, E.; Hlil, E.K. Scaling laws for the magnetocaloric effect in calicium deficiency manganites $La_{0.8}Ca_{0.2-x}\square_xMnO_3$. *J. Supercond. Nov. Magn.* **2014**, *27*, 1341–1345. [CrossRef]
4. Bhatt, R.C.; Meena, R.S.; Kishan, H.; Awana, V.P.S.; Agarwal, S.K. Magnetocaloric effect in $Ni_{47}Mn_{40}Sn_{13}$ alloy prepared by mechanical alloying. *J. Supercond. Nov. Mater.* **2016**, *29*, 3201–3206. [CrossRef]
5. Krenke, T.; Acet, M.; Wassermann, E.F.; Moya, X.; Mañosa, L.; Planes, A. Ferromagnetism in austenitic and martensitic states of Ni-Mn-In alloys. *Phys. Rev. B* **2006**, *73*, 174413. [CrossRef]
6. Yu, S.Y.; Liu, Z.H.; Liu, G.D.; Chen, J.L.; Cao, Z.X.; Wu, G.H.; Zhang, B.; Zhang, X.X. Large magnetoresistance in single-crystalline $Ni_{50}Mn_{50-x}In_x$ alloys (x= 14–16) upon martensitic transformation. *Appl. Phys. Lett.* **2006**, *89*, 162503. [CrossRef]
7. Yu, S.Y.; Gu, A.J.; Kang, S.S.; Hu, S.J.; Li, Z.C.; Ye, S.T.; Li, H.H.; Sun, J.J.; Hao, R.R. Large reversible magnetostrain in polycrystalline $Ni_{50}Mn_{33}In_{17-x}Ga_x$. *J. Alloys Compd.* **2016**, *681*, 1–5. [CrossRef]
8. Das, R.; Saravanan, P.; Arvindha Babu, D.; Perumal, A.; Srinivasan, A. Influence of solidification rate and heat treatment on magnetic refrigerant properties of melt spun $Ni_{51}Mn_{34}In_{14}Si_1$ ribbons. *J. Magn. Magn. Mater.* **2013**, *344*, 152–157. [CrossRef]
9. Das, R.; Perumal, A.; Srinivasan, A. Effect of particle size on the magnetocaloric properties of $Ni_{51}Mn_{34}In_{14}Si_1$ alloy. *J. Alloys Compd.* **2013**, *572*, 192–198. [CrossRef]
10. Şaşıoğlu, E.; Sandratskii, L.M.; Bruno, P. Role of conduction electrons in mediating exchange interactions in Mn-based Heusler alloys. *Phys. Rev. B* **2008**, *77*, 064417. [CrossRef]
11. Chaudhuri, R.G.; Paria, S. COre/Shell nanoparticles: Classes, properties, synthesis mechanisms, characterization, and applications. *Chem. Rev.* **2012**, *112*, 2373–2433. [CrossRef] [PubMed]
12. Çakır, A.; Acet, M.; Wiedwald, U.; Krenke, T.; Farle, M. Shell-ferromagnetic precipitation in martensitic off-stoichiometric Ni-Mn-In Heusler alloys produced by temper-annealing under magnetic field. *Acta Mater.* **2017**, *127*, 117–123. [CrossRef]
13. Duran, A. Surface superconductivity in $Ni_{50}Mn_{36}Sn_{14}$ Heusler alloy. *J. Supercond. Nov. Magn.* **2018**, *31*, 4053–4062. [CrossRef]
14. Freeman, A.J.; Nakamura, K.; Ito, T. Noncollinear magnetism phenomena induced at surfaces, domain walls and in votrex cores of magnetic quantum dots. *J. Magn. Magn. Mater.* **2004**, *272–276*, 1122–1127. [CrossRef]
15. Bhattacharya, K. *Microstructure of Martensit: Why It Forms and How Gives Rise to the Shape-Memory Effect*; Oxford Series on Materials Modelling; Oxford University Press: Oxford, UK, 2003; Volume 2.
16. Vasiliev, A.N.; Heczko, O.; Volkova, O.S.; Vasilchikova, T.N.; Voloshok, T.N.; Klimov, K.V.; Ito, W.; Kainuma, R.; Ishida, K.; Oikawa, K.; et al. On the electronic origin of the inverse magnetocaloric effect in Ni-Co-Mn-In Heusler alloys. *J. Phys. D Appl. Phys.* **2010**, *43*, 055004. [CrossRef]
17. Sanchez Llamazares, J.L.; Hernando, B.; Garcia, C.; González, J.; Escoda, L.; Suñol, J.J. Martensitic transformation in $Ni_{50}Mn_{34.9}In_{14.7}$ melt spun ribbons. *J. Phys. D Appl. Phys.* **2009**, *42*, 045002. [CrossRef]
18. Sanchez Llamazares, J.L.; Nedelcos, A.Q.; Ríos-Jara, D.; Sánchez-Valdes, C.F.; García-Fernández, T.; García, C. The effect of low temperature thermal annealing on the magnetic properties of Heusler Ni-Mn-Sn melt-spun ribbons. *J. Magn. Magn. Mater.* **2016**, *401*, 38–43. [CrossRef]
19. Xuan, H.C.; Deng, Y.; Wang, D.H.; Zhang, C.L.; Han, Z.D.; Du, Y.W. Effect of annealing on the martensitic transformation and magnetoresistance in Ni-Mn-Sn ribbons. *J. Phys. D Appl. Phys.* **2008**, *41*, 215002. [CrossRef]
20. Lutterotti, L.; Matthies, S.; Wenk, H.R. MAUD: A friendly Java program for material analysis using diffraction. *Newsl. CPD* **1999**, *21*, 14–15. Available online: http://maud.radiographema.com (accessed on 2 May 2021).
21. Rietveld, H.M. A profile refinement method for nuclear and magnetic structures. *J. Appl. Cryst.* **1969**, *2*, 65–71. [CrossRef]

22. Straka, L.; Hanninen, H.; Soroka, A.; Sozinov, A. Ni-Mn-Ga single crystals with very low twinning stress. *J. Phys. Conf. Ser.* **2011**, *303*, 012079. [CrossRef]
23. Weertman, J.; Weertman, J.R. *Physical Metallurgy*; Cahn, R.W., Haansen, P., Eds.; Elsevier: Amsterdam, The Netherlands, 1983; pp. 1780–1852.
24. Khatchaturyan, A.G.; Shapiro, S.M.; Semenovskaya, S. Adaptive phase formation in martensitic transformation. *Phys. Rev. B* **1991**, *43*, 10832. [CrossRef]
25. Matsuoka, Y.; Iwasaki, T.; Nakada, N.; Tsuchiyama, T.; Takaki, S. Effect of grain size on thermal and mechanical stability of austenite in metastable austenitic stainless steel. *ISIJ Int.* **2013**, *53*, 1224–1230. [CrossRef]
26. Li, Z.; Zhang, Y.; Esling, C.; Zhao, X.; Zuo, L. Evidence for a monoclinic incommensurate superstructure in modulated martensite. *Acta Mater.* **2012**, *60*, 6982–6990. [CrossRef]
27. Benacchio, G.; Titov, I.; Malayeyev, A.; Peral, I.; Mathias, B.; Bender, P.; Mettus, D.; Honecker, D.; Gilbert, E.; Coduri, M.; et al. Evidence for the formation of nanoprecipitates with magnetically disordered regions in bulk $Ni_{50}Mn_{45}In_5$ Heusler alloys. *Phys. Rev. B* **2019**, *99*, 184422. [CrossRef]
28. Krenke, T.; Moya, X.; Aksoy, S.; Acet, M.; Entel, P.; Mañosa, L.; Planes, A.; Elerman, Y.; Yücel, A.; Wassermann, E.F. Electronic aspects of the martensitic transition in Ni-Mn based Heusler alloys. *J. Magn. Magn. Mater.* **2007**, *310*, 2788–2789. [CrossRef]
29. Zheng, H.; Wu, D.; Xue, S.; Frenzel, J.; Eggeler, G.; Zhai, Q. Composition dependent crystal structure and martensitic transformation in Heusler Ni-Mn-Sn alloys. *Acta Mater.* **2011**, *59*, 5692–5699. [CrossRef]
30. Scheerbaum, N.; Hinz, D.; Gutfleisch, O.; Müller, K.H.; Schultz, L. Textured polymer bonded composites with Ni-Mn-Ga magnetic shape memory particles. *Acta Mater.* **2007**, *55*, 2707–2713. [CrossRef]
31. Dincklage, L.; Scheibel, F.; Çakır, A.; Farle, M.; Acet, M. Annealing-time and annealing-temperature dependencies of the size of Ni-Mn-In shell-ferromagnetic nano-precipitates by Scherrer analysis. *AIP Adv.* **2018**, *8*, 025012. [CrossRef]
32. Çakır, A.; Acet, M.; Farle, M. Exchange bias caused by field-induced spin reconfiguration in Ni-Mn-Sn. *Phys. Rev. B* **2016**, *93*, 094411. [CrossRef]